Volume 6 | Number 10 | December 2019 | Pages 1947–2154

Materials Horizons

rsc.li/materials-horizons

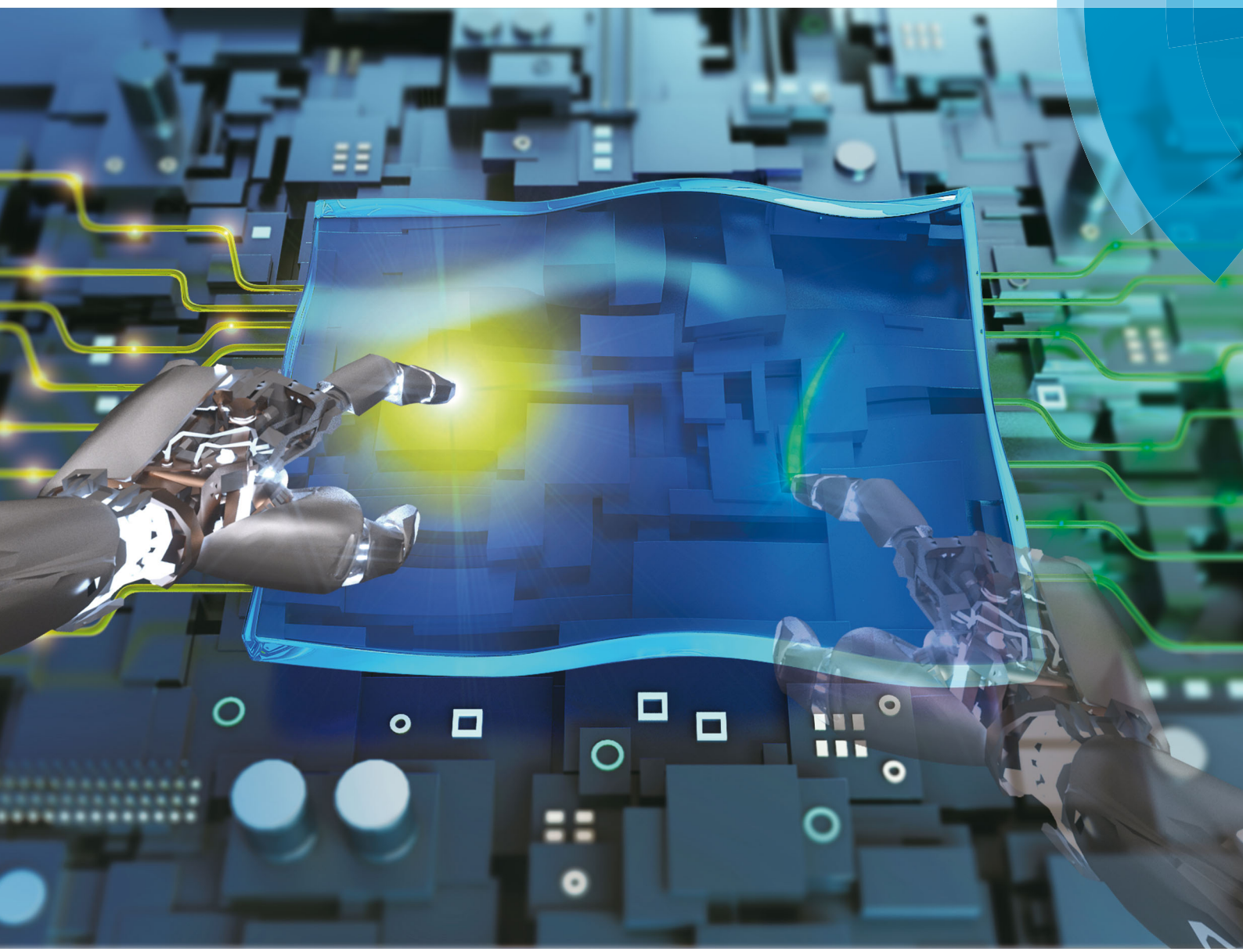

ISSN 2051-6347

ROYAL SOCIETY OF CHEMISTRY | Celebrating IYPT 2019

COMMUNICATION

Jiachi Zhang, Zhaofeng Wang *et al.*

Mechanics-induced triple-mode anticounterfeiting and moving tactile sensing by simultaneously utilizing instantaneous and persistent mechanoluminescence

Materials Horizons

COMMUNICATION

Cite this: *Mater. Horiz.*, 2019, 6, 2003

Received 3rd July 2019,
Accepted 2nd August 2019

DOI: 10.1039/c9mh01028a

rsc.li/materials-horizons

Mechanics-induced triple-mode anticounterfeiting and moving tactile sensing by simultaneously utilizing instantaneous and persistent mechanoluminescence†

Zhidong Ma,[ab] Jinyu Zhou,[a] Jiachi Zhang,*[a] Songshan Zeng,[c] Hui Zhou,[b] Andrew T. Smith,[c] Wenxiang Wang,[a] Luyi Sun[c] and Zhaofeng Wang*[b]

In this work, ultra-strong yellow and green mechanoluminescence was presented for $Y_3Al_5O_{12}:Ce^{3+}$ and $Ba_{0.5}Sr_{0.5}Si_2O_2N_2:Eu^{2+}$, respectively. In addition to the emitting color, the above materials showed distinct trap dependence/independence and spontaneous radiation behaviors, leading to instantaneous mechanoluminescence without any afterglow for $Y_3Al_5O_{12}:Ce^{3+}$ and persistent mechanoluminescence for $Ba_{0.5}Sr_{0.5}Si_2O_2N_2:Eu^{2+}$. By ingeniously combining the above unique mechanoluminescence behaviors, two types of intriguing and unprecedented devices were achieved. The devices are a mechanics-induced triple-mode anticounterfeiting device capable of displaying embedded information in varied emitting colors and dynamic patterns and a comprehensive tactile sensor that can simultaneously sense/record the contact load, motion trail, and contact position for objects moving on the surface. This work is the first to present application designs by simultaneously utilizing transient and persistent mechanoluminescence. The as-fabricated devices showed unique superiority and advancement in their own fields. Particularly, the mechanoluminescence-based tactile sensor realized comprehensive sensing functionalities within a single unit and required no extra circuit designs.

New concepts

Over the past few years, mechanoluminescence (ML) has been applied in various high-technology fields to mitigate the existing limitations. However, all related reports are based on instantaneous ML, which basically impedes its practical applications. In this work, we presented two kinds of ML materials, namely, $Y_3Al_5O_{12}:Ce^{3+}$ (YAG:Ce^{3+}) and $Ba_{0.5}Sr_{0.5}Si_2O_2N_2:Eu^{2+}$ (BSSON:Eu^{2+}), which exhibited ultra-strong instantaneous yellow ML and persistent green ML, respectively. Based on the above developed ML materials, this work is the first to simultaneously utilize transient and persistent ML. Two types of intriguing and unprecedented devices were achieved, *i.e.*, a mechanics-induced triple-mode anticounterfeiting device and a comprehensive tactile sensor. In particular, the as-fabricated tactile sensor overcame the challenge to simultaneously achieve the spatial sensing of contact load/press and the real-time tracking of the contact position by a single sensor without any extra circuit design. This work offers clear guidance for persistent ML materials for various advanced applications. We believe that researchers in the related fields including flexible electronics and sensors will significantly benefit from the principles disclosed in this report.

1. Introduction

Mechanoluminescence (ML) refers to the light-emitting behavior of materials by applying mechanical stimuli.[1] As one of the oldest forms of luminescence, the phenomenon of ML was recorded in ancient times, *e.g.*, light-emitting accompanied by an earthquake.[2] However, most of the observed ML in the early stages was caused by the fracture of materials or crystals. Together with the limitation of detection methods, ML was considered to be useless for a long time.[3] Due to the development of photomultipliers and the realization of structural non-destructive ML, the research on ML has regained attention during the past decades and shown enormous potential applications in various frontier domains.[4–11]

At present, the research on ML mainly focuses on the exploitation of high-performance materials with respect to high brightness and excellent mechanical cycling stability.[12,13] The most representative ML system is transition metal-doped zinc sulfide (ZnS: Mn/Cu), which shows brightness of *ca.* 120 cd cm^{-2} with no degradation even after 10 000 cycles of mechanical tests.[14] However, sulfur sources participate in the synthesis of ZnS-based materials, which causes serious environmental pollution. In addition, the lack of abundant energy levels in the luminescent centers in ZnS: Mn/Cu restricts the emitting color. Therefore, it is urgent for researchers to develop novel and highly efficient ML systems, which are environmentally friendly and have abundant radiative transfer channels for various emitting colors.

[a] *National & Local Joint Engineering Laboratory for Optical Conversion Materials and Technology, Lanzhou University, Lanzhou 730000, P. R. China. E-mail: zhangjch@lzu.edu.cn*

[b] *State Key Laboratory of Solid Lubrication, Lanzhou Institute of Chemical Physics, Chinese Academy of Sciences, Lanzhou 730000, P. R. China. E-mail: zhfwang@licp.cas.cn*

[c] *Polymer Program, Institute of Materials Science and Department of Chemical & Biomolecular Engineering, University of Connecticut, Storrs, Connecticut 06269, USA*

† Electronic supplementary information (ESI) available. See DOI: 10.1039/c9mh01028a

Because ML materials directly establish the relationship between mechanics and luminescence, they have been further applied in various high-technology fields with the expectation to mitigate their limitations.[15–22] For example, ZnS-based ML materials have been used to fabricate advanced devices for the applications of wind-driven lighting and display,[23] personalized handwriting,[24] skin movement recognition,[25] energy/information storage,[26,27] *etc.* In our previous work,[28] the dynamic stress responsiveness of ML was also utilized to achieve a comprehensive stretching/strain sensor capable of sensing both strain level and stretching states. It should be noted that the employed ML in previous studies was actually instantaneous luminescence with a short duration time in the range from nanoseconds (ns) to microseconds (ms).[29–31] This basically impeded the practical applications of ML although further device designs may alleviate the problems to a certain extent. For most inorganic compounds, ML is generated by the intrinsic energy difference,[32] and it is impossible for researchers to achieve steady ML by just controlling the applied mechanical energy. However, it is reasonable to prolong the ML to achieve persistent ML or ML afterglow in inorganic materials by utilizing intrinsic energy saving and spontaneous emission activities, which are similar to those in long-lasting phosphors.[33] According to inorganic long persistence principles, ML with afterglow should fulfill the following aspects:[34,35] (i) there should be abundant traps with various depths in the structure; (ii) the deep traps should transfer their energy directly to the luminescent centers or to the shallow traps; (iii) the energy in the shallow traps must spontaneously transfer to the radiative energy levels to generate luminescence. One can conclude that the simultaneous utilization of the transient ML and ML afterglow can fill in the gaps in the present ML research, thus bringing revolutionary applications.[36]

Inspired by the above considerations, we presented two types of materials, namely, $Y_3Al_5O_{12}:Ce^{3+}$ ($YAG:Ce^{3+}$) and $Ba_{0.5}Sr_{0.5}Si_2O_2N_2:Eu^{2+}$ ($BSSON:Eu^{2+}$), which exhibited ultra-strong ML with yellow and green emissions, respectively. The employment of $YAG:Ce^{3+}$ and $BSSON:Eu^{2+}$ was based on their sensitivity to the applied stress as well as the intrinsic efficient radiative transfer channels.[37–39] In addition, $BSSON:Eu^{2+}$ has already been demonstrated to possess deep and shallow traps in its structure with the transfer of the trapped carriers fulfilling the aforementioned conditions for ML afterglow.[37,40] As a result, after applying mechanical stimuli like rubbing, pressing, and stretching, the green ML of $BSSON:Eu^{2+}$ could last for tens of seconds. Because of the co-existence of Ba^{2+} and Ca^{2+}, $BSSON:Eu^{2+}$ showed an enhanced ML persistence performance compared to $BaSi_2O_2N_2:Eu^{2+}$.[37] By ingeniously combining the transient ML of $YAG:Ce^{3+}$ and the persistent ML of $BSSON:Eu^{2+}$ as well as their distinct ML colors, a mechanics-induced triple-mode anticounterfeiting device implanted with bar codes was developed. It could display varied ML colors and dynamic ML patterns when mechanically stimulated, greatly elevating the anticounterfeiting level. Furthermore, because of the introduction of the ML afterglow of $BSSON:Eu^{2+}$, an intriguing tactile sensor for moving objects on the surface was fabricated, which could simultaneously sense/record the contact load, motion trail, and contact position in a single unit without any extra circuit designs. This comprehensive tactile sensor shows potential applications for mechanics monitoring, human-machine interfacing, and intelligent artificial skin.

2. Results and discussion

The crystal structure, morphology, and element distribution of $YAG:Ce^{3+}$ and $BSSON:Eu^{2+}$ powders were studied by X-ray diffraction (XRD), scanning electron microscopy (SEM) and high-resolution transmission electron microscopy (HR-TEM), as shown in Fig. S1 and S2 (ESI†). The corresponding results suggested that both $YAG:Ce^{3+}$ and $BSSON:Eu^{2+}$ were of a single phase with the dopants (Ce^{3+}/Eu^{2+}) homogeneously distributed in the matrices. To facilitate the characterization and analysis of ML from the above powders, they were further composited in a polydimethylsiloxane (PDMS) elastomer because of its efficient stress transfer ability, softness/stretchability, and high optical transparency.[15] Fig. 1a–c show the schematic and cross-section SEM images of the as-fabricated ML elastomers. It was observed that the thickness of the composite elastomer was *ca.* 582.8 μm with ML particles well-dispersed in the PDMS matrix. When the elastomers were stimulated by mechanics such as pressing, rubbing, stretching, tearing, and folding, intense yellow and green ML could be observed for $YAG:Ce^{3+}$/PDMS and $BSSON:Eu^{2+}$/PDMS, respectively, as presented in Fig. 1d. Based on the stretching-induced ML of a series of $YAG:xCe^{3+}$ (x = 0.01, 0.015, 0.02, 0.025, 0.03) and $BSSON:yEu^{2+}$ (y = 0.03, 0.04, 0.05, 0.06, 0.07), as shown in Fig. S3 (ESI†), the optimal samples were determined to be $YAG:2.5\%Ce^{3+}$ and $BSSON:6\%Eu^{2+}$,

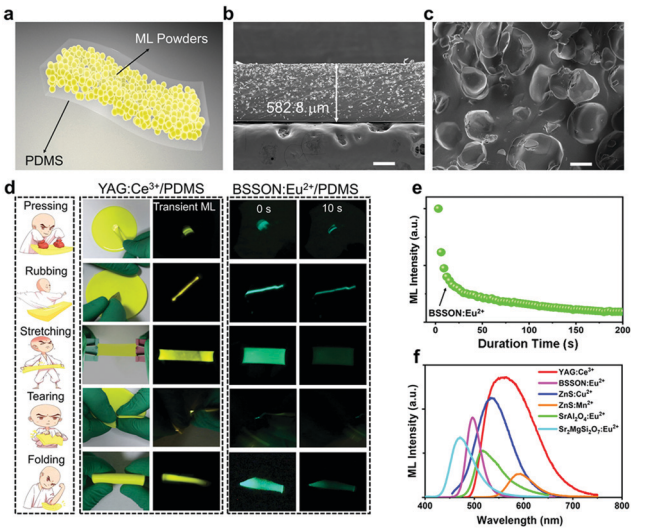

Fig. 1 (a) A general schematic of the ML composite. (b and c) Cross-section SEM images of the as-fabricated $YAG:Ce^{3+}$/PDMS composites in low magnification (scale bar: 200 μm) and high magnification (scale bar: 10 μm). (d) Schematic and optical photographs of ML from $YAG:Ce^{3+}$/PDMS and $BSSON:Eu^{2+}$/PDMS composites under the stimuli of pressing, rubbing, stretching, tearing, and folding. (e) ML duration time of $BSSON:Eu^{2+}$ after stopping the mechanical stimulus. (f) Comparison of the ML spectra of $BSSON:Eu^{2+}$, $YAG:Ce^{3+}$, ZnS: Cu^{2+}, $ZnS:Mn^{2+}$, $SrAl_2O_4:Eu^{2+}$ and $Sr_2MgSi_2O_7:Eu^{2+}$ composited in the PDMS elastomers.

respectively. The emitted ML showed a linear relationship between the mechanical stimulus and emission intensity (Fig. S4, ESI†), demonstrating their potential applications for mechanical sensors. In addition to the emitting color, it was attractive to find that YAG:Ce^{3+} and BSSON:Eu^{2+} exhibited distinct ML afterglow behaviors: YAG:Ce^{3+} displayed transient ML in PDMS (the ML duration time after stopping the mechanical stimulus was beyond the lower detection limit (10 ms) of our CCD camera), while the ML of BSSON:Eu^{2+} lasted for tens of seconds (Fig. 1e). The real ML observations under various mechanical stimuli from YAG:Ce^{3+} and BSSON:Eu^{2+} are presented in Movies S1–S5 (ESI†). By comparing the ML spectra of YAG:Ce^{3+} and BSSON:Eu^{2+} with those of the well-studied ML materials of ZnS:Cu^{2+}, ZnS:Mn^{2+}, $SrAl_2O_4$:Eu^{2+} and $Sr_2MgSi_2O_7$:Eu^{2+} measured at the same tensile conditions (Fig. 1f; ML powder composition: 64.5 wt%; elastomer dimension: 44 mm (length) × 17 mm (width) × 0.58 mm (thickness); stretching speed: 960 mm min^{-1}; tensile strain: 36%), it was confirmed that YAG:Ce^{3+} showed the most intense ML, which was even 64% higher than that of ZnS:Cu^{2+}. The ML spectra of all samples were consistent with their photoluminescence (PL) spectra (Fig. S5, ESI†), suggesting that both the ML and PL of the samples possessed the same emission processes for the electron–hole recombination within the luminescent centers.

Since the ML emission processes of both BSSON:Eu^{2+} and YAG:Ce^{3+} originate from the radiative transfer within the luminescent centers, the differences between their PL and ML should lie in the excitation/activation and energy transfer pathways. The red curves in Fig. 2a and c show the thermoluminescence (ThL) spectra of BSSON:Eu^{2+} and YAG:Ce^{3+}, respectively, after 365 nm light irradiation for 5 min, confirming the existence of trap levels in the structure with energy storage ability (the details are presented in Fig. S6, ESI†).[41–44] The stored energy could be further released after a thermal treatment, which could be totally cleared at the temperatures of 523 K and 680 K for BSSON:Eu^{2+} and YAG:Ce^{3+}, respectively (blue curves in Fig. 2a and c). To determine whether there was a relationship between ML and the trapped energy in the structure, the ML variations of the BSSON:Eu^{2+}- and YAG:Ce^{3+}-based elastomers after various temperature treatments were investigated. As shown in Fig. 2b, the ML intensity of BSSON:Eu^{2+} gradually decreases with the increase in temperature and completely disappears at 523 K. This was consistent with the varying trend for the trapped energy, supporting that the ML of BSSON:Eu^{2+} originated from the release of the trapped energy. The ML degradation of BSSON:Eu^{2+} under cycle tests and the ML quick recovery property under ultraviolet (UV) light irradiation, as shown in Fig. 2e, further demonstrated the above viewpoint. Considering the fact that the irradiation-stimulated persistent luminescence of BSSON:Eu^{2+} was fully eliminated before the ML tests, the specific ML mechanisms of BSSON:Eu^{2+} including the ML afterglow were concluded, as shown in Fig. 2g. Under mechanical stimulation, the energy stored in the deep traps of BSSON:Eu^{2+} could be released and transferred to the luminescent centers to produce ML, part of which was transferred to the shallow traps to produce spontaneous emission, namely, ML afterglow.

For YAG:Ce^{3+}, the ML mechanism was totally different from that of BSSON:Eu^{2+}. The ML of YAG:Ce^{3+} exhibited a temperature-independent behavior, as shown in Fig. 2d. Although it also showed degradation under the cycle tests, the ML intensity could not be quickly recovered by filling the energy in traps using UV light irradiation (Fig. 2e). All the above phenomena suggested that the ML of YAG:Ce^{3+} did not originate from the trapped energy in the structure. By combining the trap-independent behavior, ML degradation under the cycle tests, and the phonon density variation after mechanical stimulation revealed by Raman spectra (Fig. S7, ESI†), a possible ML mechanism for YAG:Ce^{3+} involving the phonon-assisted mechanical energy transfer processes was proposed. As shown in Fig. 2h, under the stimulation of stress, the electrons at the ground level of Ce^{3+} could be transferred to the excited levels with the assistance of the energy from the phonons in the matrix, which then recombined with the holes to produce luminescence. The observed ML self-recovery characteristic of YAG:Ce^{3+} in the dark under an ambient environment (Fig. 2f) further demonstrated the proposed phonon-assisted ML mechanism.

Since BSSON:Eu^{2+} and YAG:Ce^{3+} displayed distinct ML colors, trap-dependent/independent behaviors, and ML afterglow, they were utilized to fabricate a mechanics-induced triple-mode anticounterfeiting device. The fabrication processes were simple and facile, as illustrated in Fig. 3a. First, the BSSON:Eu^{2+}/PDMS and YAG:Ce^{3+}/PDMS elastomers were cut into strips with the designated widths. Then, the strips were placed into a Petri dish (diameter: 60 mm) filled with the PDMS precursor. After curing at 80 °C for 2 h, an anticounterfeiting device with ML bar codes was obtained (Fig. 3b). Before the anticounterfeiting test, the device

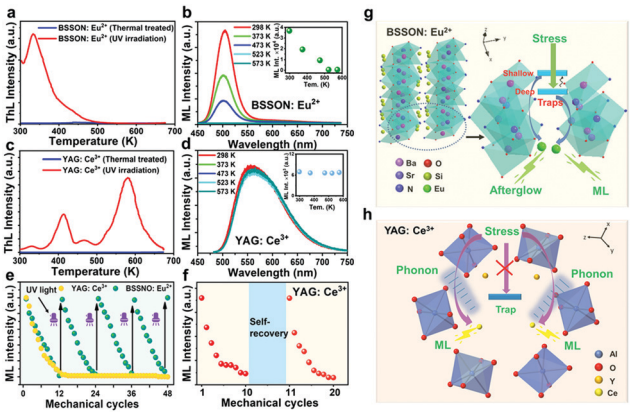

Fig. 2 (a) ThL spectra of BSSON:Eu^{2+} after the treatments of 365 nm UV light irradiation for 5 min and 523 K for 10 min. (b) ML intensity of the BSSON:Eu^{2+}/PDMS elastomer *vs.* the treated temperature. (c) ThL spectra of YAG:Ce^{3+} after the treatments of 365 nm UV light irradiation for 5 min and 680 K for 10 min. (d) ML intensity of the YAG:Ce^{3+}/PDMS elastomer *vs.* the treated temperature. (e) Cycle stability tests of the stretching-induced ML of BSSON:Eu^{2+} and YAG:Ce^{3+} in PDMS with and without UV irradiation (elastomer dimension: 44 mm (length) × 17 mm (width) × 0.58 mm (thickness); stretching speed: 960 mm min^{-1}; tensile strain: 36%). (f) ML intensity degradation of the YAG:Ce^{3+}/PDMS elastomer along with the continuous increase in the stretching cycles and its ML self-recovery property after placing the elastomer in the dark under an ambient environment for 48 h (the ML measurement conditions were the same as those in (e)). Schematic diagrams for the ML processes of (g) BSSON:Eu^{2+} and (h) YAG:Ce^{3+}.

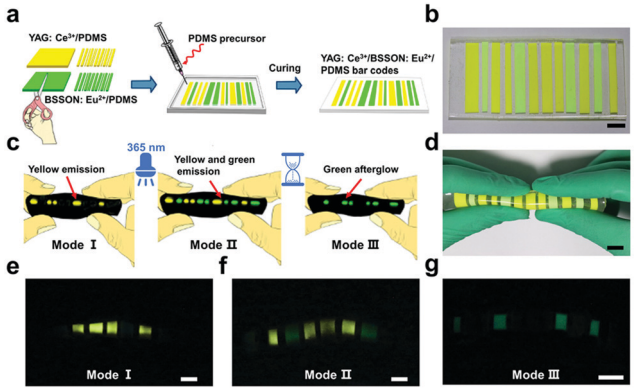

Fig. 3 (a) Fabricating processes and (b) optical photograph of the mechanics-induced triple-mode anticounterfeiting elastomer, scale bar: 1 cm. (c) Schematics and (d–g) optical photographs of the triple-mode ML-based anticounterfeiting patterns in the dark under an ambient environment, scale bar: 1 cm.

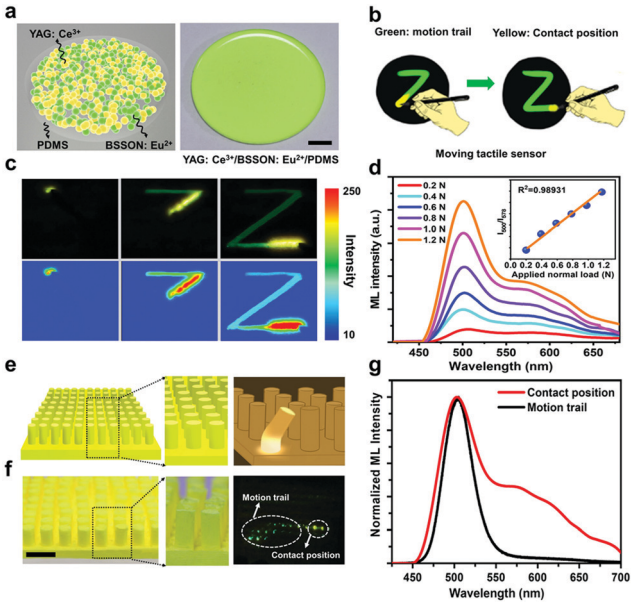

Fig. 4 (a) Schematic and optical photograph of the as-fabricated tactile sensor, scale bar: 1 cm. (b) Illustration of the contact tracking effects for both motion trail and contact position by writing a letter "Z" on the device surface. (c) Real contact tracking photos and luminescent mappings of the device. (d) ML spectra of the contact position of the as-fabricated tactile sensor under various contact loads; the inset shows the corresponding green (500 nm) to yellow (578 nm) ML intensity ratio *vs.* applied normal load. (e) Schematic and (f) optical photographs of the array-based tactile sensor, scale bar: 5 mm. (g) Normalized ML spectra measured from the motion trail and contact position on the array-based tactile sensor.

was thermally treated to clean the traps in the structure. When stimulated by folding under an ambient environment, the device just displayed yellow ML for YAG:Ce^{3+} (mode I) because of its trap-independent characteristic (Fig. 3c). However, after the device was irradiated by a 365 nm light for 5 min to fill energy in the traps, green ML of BSSON:Eu^{2+} appeared and the device exhibited instantaneous bar code patterns with both green and yellow colors by folding (mode II). Because YAG:Ce^{3+} and BSSON:Eu^{2+} exhibited short and long ML duration times after stopping the mechanical stimuli, respectively, the device then showed only the green bar code patterns of BSSON:Eu^{2+} (mode III). The real photos and video for the above-mentioned triple-mode anticounterfeiting are presented in Fig. 3d–g and Movie S6 (ESI†). As a result, we successfully achieved a mechanics-induced triple-mode anticounterfeiting device by combining the distinct ML properties of YAG:Ce^{3+} and BSSON:Eu^{2+}; also, it was facile to prepare and operate. In addition to overcoming the limitation of the anticounterfeiting modes by the traditional PL methods,[45–47] the as-fabricated device could further implant various anticounterfeiting information by designing the patterns or the widths of the bar codes, elevating the security level of the present anticounterfeiting technology.

In addition to the triple-mode anticounterfeiting based on the folding-induced ML of YAG:Ce^{3+} and BSSON:Eu^{2+}, their rubbing-induced ML was also utilized to realize a comprehensive tactile sensor for moving objects on a surface. Fig. 4a shows the schematic and optical photograph of the as-fabricated device; the YAG:Ce^{3+} and BSSON:Eu^{2+} powders were mechanically mixed together in a PDMS matrix. Because of the combination of the instantaneous yellow ML of YAG:Ce^{3+} and the persistent green ML of BSSON:Eu^{2+}, it was expected that when a contact object moved on the surface, the motion trail and contact position would exhibit a distinct ML color, *i.e.*, green ML afterglow for the motion trail and greenish yellow ML (the combination of green and yellow ML) for the contact position, respectively (Fig. 4b). Fig. 4c and Fig. S8, Movie S7 (ESI†) show the real photos and video of the tactile sensing by writing a letter "Z" on the surface of the device, confirming the contact tracking effects of our device. Moreover, the greenish yellow ML from the contact position showed a linear relationship between the I_{500}/I_{578} ratio (the ML intensity ratio of green emission at 500 nm to yellow emission at 578 nm) and the contact load in the range from 0.2 to 1.2 N, as shown in Fig. 4d. Therefore, the as-fabricated YAG:Ce^{3+}/BSSON:Eu^{2+}/PDMS-based device was demonstrated to simultaneously sense/record the contact load, motion trail, and contact position for the object moving on a surface. To further improve the contact tracking accuracy, uniform YAG:Ce^{3+}/BSSON:Eu^{2+}/PDMS arrays were designed on the surface of the device (diameter: 2 mm, height: 5 mm, array spacing: 1 mm) by a commercial desktop 3D printer (Raise3D N2), as presented in Fig. 4e–g. The elastic array design facilitated the stress transfer from PDMS to the ML powders, endowing the device with high luminescence efficiency and controllable pixels.

For general tactile sensors, the basic functionality is to sense the applied load/press in a reasonable range.[48,49] In previous reports, great efforts, such as the integration of electrical signal-based tactile sensors on a circuit board, have been made to allow the device to sense the spatial load/press distribution and the real-time tracking of the contact position.[50–52] The tactile sensor developed in this work by simultaneously utilizing instantaneous and persistent mechanoluminescence achieved the above functionalities in a single unit without any extra circuit design. Significantly, the spatial load/press distribution, motion trail, and contact position could be simply distinguished

by directly observing the exhibited visible ML. This tactile sensor can be promisingly applied in mechanics monitoring, human-machine interfacing, intelligent artificial skin, and other related fields.

3. Conclusions

In summary, we demonstrated ultra-strong yellow instantaneous ML in YAG:Ce^{3+} and green persistent ML in BSSON:Eu^{2+}. By studying trap dependence/independence, spontaneous radiation, and recovery behaviors, different underlying ML mechanisms were proposed. Based on the distinct properties of YAG:Ce^{3+} and BSSON:Eu^{2+} in terms of ML color and ML afterglow, mechanics-induced triple-mode anticounterfeiting was realized, which can greatly elevate the security level of the present anticounterfeiting technology. Furthermore, a comprehensive tactile sensor was fabricated, which could simultaneously sense the contact load, motion trail, and contact position for the objects moving on a surface, thus showing promising applications in mechanics monitoring, human-machine interfacing, intelligent artificial skin, and other related fields.

Conflicts of interest

There are no conflicts to declare.

Acknowledgements

Z. W. acknowledges the support from the CAS Pioneer Hundred Talents Program. J. Z. is grateful for the support from the National Natural Science Foundation of China (No. 10904057) and the Science and Technology Projects of Gansu Province (No. 18JR3RA270).

Notes and references

1 A. J. Walton, *Adv. Phys.*, 1977, **26**, 887–948.
2 Y. Xie and Z. Li, *Chem*, 2018, **4**, 943–971.
3 D. Peng, B. Chen and F. Wang, *ChemPlusChem*, 2015, **80**, 1209–1215.
4 C.-N. Xu, T. Watanabe, M. Akiyama and X.-G. Zheng, *Appl. Phys. Lett.*, 1999, **74**, 2414–2416.
5 S. M. Jeong, S. Song, S.-K. Lee and N. Y. Ha, *Adv. Mater.*, 2013, **25**, 6194–6200.
6 J. S. Kim and G.-W. Kim, *Sens. Actuators, A*, 2014, **218**, 125–131.
7 M.-C. Wong, L. Chen, M.-K. Tsang, Y. Zhang and J. Hao, *Adv. Mater.*, 2015, **27**, 4488–4495.
8 Y. Du, Y. Jiang, T. Sun, J. Zhao, B. Huang, D. Peng and F. Wang, *Adv. Mater.*, 2019, **31**, 1807062.
9 Q. Guo, B. Huang, C. Lu, T. Zhou, G. Su, L. Jia and X. Zhang, *Mater. Horiz.*, 2019, **6**, 996–1004.
10 J.-C. Zhang, C.-N. Xu, S. Kamimura, Y. Terasawa, H. Yamada and X. Wang, *Opt. Express*, 2013, **21**, 12976–12986.
11 L. Li, L. Wondraczek, L. Li, Y. Zhang, Y. Zhu, M. Peng and C. Mao, *ACS Appl. Mater. Interfaces*, 2018, **10**, 14509–14516.
12 J.-C. Zhang, Y.-Z. Long, X. Yan, X. Wang and F. Wang, *Chem. Mater.*, 2016, **28**, 4052–4057.
13 D. Tu, C.-N. Xu, A. Yoshida, M. Fujihala, J. Hirotsu and X.-G. Zheng, *Adv. Mater.*, 2017, **29**, 1606914.
14 S. M. Jeong, S. Song, S.-K. Lee and B. Choi, *Appl. Phys. Lett.*, 2013, **102**, 051110.
15 S. M. Jeong, S. Song, H. Kim, K.-I. Joo and H. Takezoe, *Adv. Funct. Mater.*, 2016, **26**, 4848–4858.
16 S. M. Jeong, S. Song and H. Kim, *Nano Energy*, 2016, **21**, 154–161.
17 N. Terasaki, H. Yamada and C.-N. Xu, *Catal. Today*, 2013, **201**, 203–208.
18 L. Chen, M.-C. Wong, G. Bai, W. Jie and J. Hao, *Nano Energy*, 2015, **14**, 372–381.
19 J.-C. Zhang, C. Pan, Y.-F. Zhu, L.-Z. Zhao, H.-W. He, X. Liu and J. Qiu, *Adv. Mater.*, 2018, **30**, 1804644.
20 H. Fang, X. Wang, Q. Li, D. Peng, Q. Yan and C. Pan, *Adv. Energy Mater.*, 2016, **6**, 1600829.
21 H. Xu, F. Wang, Z. Wang, H. Zhou, G. Zhang, J. Zhang, J. Wang and S. Yang, *Tribol. Lett.*, 2018, **67**, 13.
22 X. Wang, D. Peng, B. Huang, C. Pan and Z. L. Wang, *Nano Energy*, 2019, **55**, 389–400.
23 S. M. Jeong, S. Song, K.-I. Joo, J. Kim, S.-H. Hwang, J. Jeong and H. Kim, *Energy Environ. Sci.*, 2014, **7**, 3338–3346.
24 X. Wang, H. Zhang, R. Yu, L. Dong, D. Peng, A. Zhang, Y. Zhang, H. Liu, C. Pan and Z. L. Wang, *Adv. Mater.*, 2015, **27**, 2324–2331.
25 X. Qian, Z. Cai, M. Su, F. Li, W. Fang, Y. Li, X. Zhou, Q. Li, X. Feng, W. Li, X. Hu, X. Wang, C. Pan and Y. Song, *Adv. Mater.*, 2018, **30**, 1800291.
26 Y. Zuo, X. Xu, X. Tao, X. Shi, X. Zhou, Z. Gao, X. Sun and H. Peng, *J. Mater. Chem. C*, 2019, **7**, 4020–4025.
27 D. K. Patel, B.-E. Cohen, L. Etgar and S. Magdassi, *Mater. Horiz.*, 2018, **5**, 708–714.
28 C. Wu, S. Zeng, Z. Wang, F. Wang, H. Zhou, J. Zhang, Z. Ci and L. Sun, *Adv. Funct. Mater.*, 2018, **28**, 1803168.
29 R. Sharma, D. P. Bisen, S. J. Dhoble, N. Brahme and B. P. Chandra, *J. Lumin.*, 2011, **131**, 2089–2092.
30 B. P. Chandra, S. Parganiha, V. K. Chandra, P. Jha and R. N. Baghel, *Sens. Actuators, A*, 2015, **235**, 203–209.
31 G. Qiu, H. Ye, X. Wang, H. Fang, Y. Li and X. Yao, *Ceram. Int.*, 2019, **45**, 8553–8560.
32 J.-C. Zhang, X. Wang, G. Marriott and C.-N. Xu, *Prog. Mater. Sci.*, 2019, **103**, 678–742.
33 W. Wang, Z. Sun, X. He, Y. Wei, Z. Zou, J. Zhang, Z. Wang, Z. Zhang and Y. Wang, *J. Mater. Chem. C*, 2017, **5**, 4310–4318.
34 Y. Li, M. Gecevicius and J. Qiu, *Chem. Soc. Rev.*, 2016, **45**, 2090–2136.
35 F. Clabau, X. Rocquefelte, T. Le Mercier, P. Deniard, S. Jobic and M. H. Whangbo, *Chem. Mater.*, 2006, **18**, 3212–3220.
36 J.-A. Li, J. Zhou, Z. Mao, Z. Xie, Z. Yang, B. Xu, C. Liu, X. Chen, D. Ren, H. Pan, G. Shi, Y. Zhang and Z. Chi, *Angew. Chem., Int. Ed.*, 2018, **57**, 6449–6453.
37 J. Botterman, K. V. d. Eeckhout, I. D. Baere, D. Poelman and P. F. Smet, *Acta Mater.*, 2012, **60**, 5494–5500.
38 Y. Gu, Q. Zhang, Y. Li and H. Wang, *J. Mater. Chem.*, 2010, **20**, 6050–6056.

39 V. Bachmann, C. Ronda and A. Meijerink, *Chem. Mater.*, 2009, **21**, 2077–2084.
40 M. Wang, X. Zhang, Z. Hao, X. Ren, Y. Luo, H. Zhao, X. Wang and J. Zhang, *J. Electrochem. Soc.*, 2010, **157**, H178–H181.
41 R. Chen, *J. Electrochem. Soc.*, 1969, **116**, 1254–1257.
42 G. Kitis, J. M. Gomez-Ros and J. W. N. Tuyn, *J. Phys. D: Appl. Phys.*, 1998, **31**, 2636–2641.
43 Y. Jiang, F. Wang, H. Zhou, Z. Fan, C. Wu, J. Zhang, B. Liu and Z. Wang, *Mater. Sci. Eng., C*, 2018, **92**, 374–380.
44 A. Feng and P. F. Smet, *Materials*, 2018, **11**, 484.
45 K. Jiang, L. Zhang, J. Lu, C. Xu, C. Cai and H. Lin, *Angew. Chem., Int. Ed.*, 2016, **55**, 7231–7235.
46 J. Andres, R. D. Hersch, J.-E. Moser and A.-S. Chauvin, *Adv. Funct. Mater.*, 2014, **24**, 5029–5036.
47 D. Zhang, W. Zhou, Q. Liu and Z. Xia, *ACS Appl. Mater. Interfaces*, 2018, **10**, 27875–27884.
48 X. Wang, M. Que, M. Chen, X. Han, X. Li, C. Pan and Z. L. Wang, *Adv. Mater.*, 2017, **29**, 1605817.
49 Q. Hua, J. Sun, H. Liu, R. Bao, R. Yu, J. Zhai, C. Pan and Z. L. Wang, *Nat. Commun.*, 2018, **9**, 244.
50 W. Wu, X. Wen and Z. L. Wang, *Science*, 2013, **340**, 952.
51 X. Wang, H. Zhang, L. Dong, X. Han, W. Du, J. Zhai, C. Pan and Z. L. Wang, *Adv. Mater.*, 2016, **28**, 2896–2903.
52 Z. W. Yang, Y. Pang, L. Zhang, C. Lu, J. Chen, T. Zhou, C. Zhang and Z. L. Wang, *ACS Nano*, 2016, **10**, 10912–10920.

